THE PROPAGATION OF *Pn* IN WESTERN CHINA

Robert L. Nowack[1], Wang-Ping Chen[2], Jessica D. Griffin[1], Ali C. Bakir[1] and Tai-Lin Tseng[2]

Purdue University[1] and University of Illinois[2]

Sponsored by the Air Force Research Laboratory

Award No. FA8718-08-C-0025
Proposal No. BAA08-42

ABSTRACT

The propagation of *Pn* in Western China is investigated with regional events recorded by the Himalyan-Tibetan Continental Lithosphere during Mountain Building (Hi-CLIMB) array in Tibet. Seismic attributes, including arrival times, Hilbert envelope amplitudes, and instantaneous and spectral frequencies, are used to study how the crustal and upper-mantle velocity and attenuation structure affects the propagation of *Pn* arrivals in Tibet. We have constructed more than 30 high-quality regional seismic profiles, and of these, 12 events have been selected with excellent crustal and *Pn* arrivals for further analysis. Regional travel times recorded by the Hi-CLIMB array are utilized to constrain the large-scale velocity structure in the region, with four near regional events to the array used to constrain the crustal structure. The travel times from the far regional events indicate that the Moho beneath the southern Lhasa terrane is up to 75 km thick, with *Pn* velocities greater than 8 km/s. In contrast, the data sampling the Qiangtang terrane north of the Bangong-Nujiang suture shows thinner crust with Pn velocities less than 8 km/s. This is consistent with the virtual seismic profile results of Tseng et al. (2009) of the teleseismic *SsPmp* phase recorded along the Hi-CLIMB array. Nonetheless, there is additional variability of the regional travel-time data suggesting further 3D complexities. Seismic amplitude and frequency attributes have been extracted from the crustal and *Pn* wave trains, and these data are compared with numerical results for models with upper-mantle velocity gradients and attenuation, which can strongly affect *Pn* amplitudes and pulse frequencies. The numerical modeling is performed using the complete spectral element method (SEM), where the results from the SEM method are in good agreement with analytical and reflectivity results for different models with upper-mantle velocity gradients. The approach we are following is to have the analysis of *Pn* seismic attributes be largely data driven to investigate the effects of large-scale lithospheric structure, velocity gradient heterogeneities, and attenuation in Tibet.

OBJECTIVES

We are investigating the propagation of regional *Pn* waves recorded by the Hi-CLIMB array in Tibet. Considering the station spacing (3 to 8 km) and large aperture (800 km) of the Hi-CLIMB seismic experiment, our objective is to use these densely recorded data to construct a self-consistent model of *Pn* propagation over a large region in western China. In turn, a better understanding of the effects of *Pn* propagation from analysis of the data will improve frequency-dependent attenuation models of regional *Pn* phases. This will lead to a clearer separation of elastic and anelastic effects in a laterally varying crust and upper mantle, eventually eliminating the assumption of a simplified, frequency-independent geometric spreading component.

RESEARCH ACCOMPLISHED

We have constructed more than 30 high-quality seismic profiles recorded on the Tibet Hi-CLIMB array (Nabelek, et al., 2005) and from these, 12 have been selected for further analysis. Similarities in the seismic profiles for events in clusters are outstanding. About two-thirds of the larger earthquakes have fault-plane solutions available in the global Harvard Centroid Moment Tensor (CMT) catalog (Dziewonski et al., 1981) and the report by Baur (2007). For those without fault plane solutions, we have identified several additional events that can be resolved using regional waveforms recorded by Hi-CLIMB stations for their appropriate azimuthal coverage. The fault-plane solutions that cannot be obtained through this method have been estimated based on geologic structures or historic solutions.

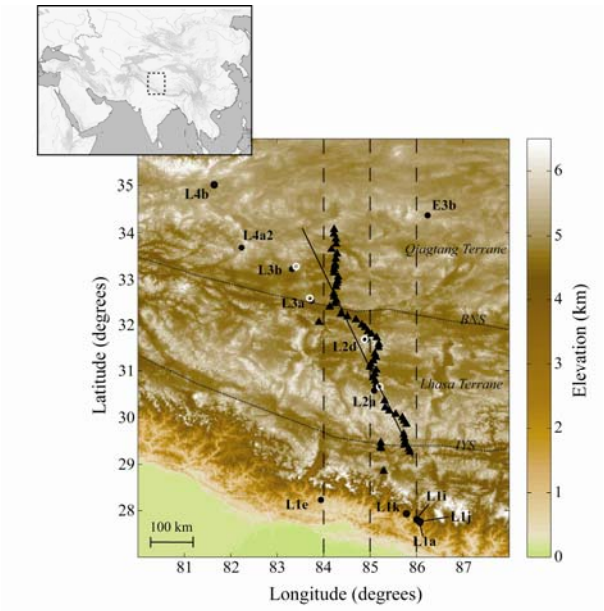

Figure 1. Map of the stations of the Hi-CLIMB array in Tibet (triangles) and the epicenters of the selected regional earthquake sources (circles). Black circles are the hypocenters reports by the PDE catalogs and Engdahl et al. (1998), and the white circles are the epicenters nearest to the array that have been relocated in this study. The dashed lines indicate the locations of north-south slices of the P-wave velocities from travel-time modeling, with the East Line at 84 degrees, the Central Line at 85 degrees, and the West Line at 86 degrees in longitude.

Regional events recorded by the Tibet Hi-CLIMB array with locations approximately in line with the array have been chosen for analysis here and are shown in Figure 1. However, other events in specific terranes have also been identified for later processing. Four of the in-line events have epicenters less than 200 km from the Hi-CLIMB array, and these events were relocated with data from the Hi-CLIMB array using the earthquake location program HYPOINVERSE-2000 (Klein, 2002). The locations of selected in-line events are shown in Figure 1, using the Engdahl et al. (1998) or the Preliminary Determination of Epicenters (PDE) catalogs for all events except the four nearby events (L2a, L2d, L3a, and L3b), which were relocated using Hi-CLIMB data. These relocations improved the fit to the travel-times but moved the epicenters on average of about 5 km. For more-distant events in Tibet, a

focal depth normalization procedure was used since events on the Tibetan plateau are dominantly less than 15 km in focal depth (e.g., Molnar and Chen, 1983; Chen and Molnar, 1983; Langin et al., 2003).

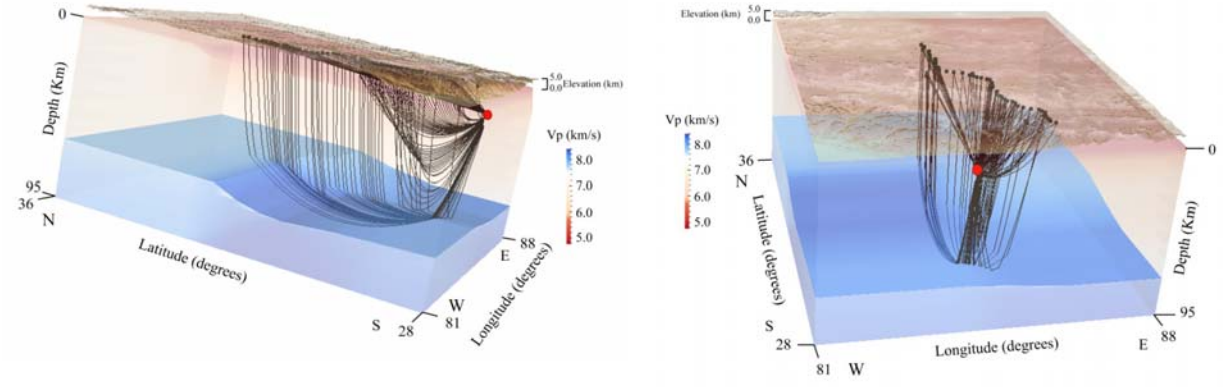

Figure 2. Ray diagrams calculated using the 3D ray-tracer cathode ray tube (CRT) for the Event L1E located by the red dot.

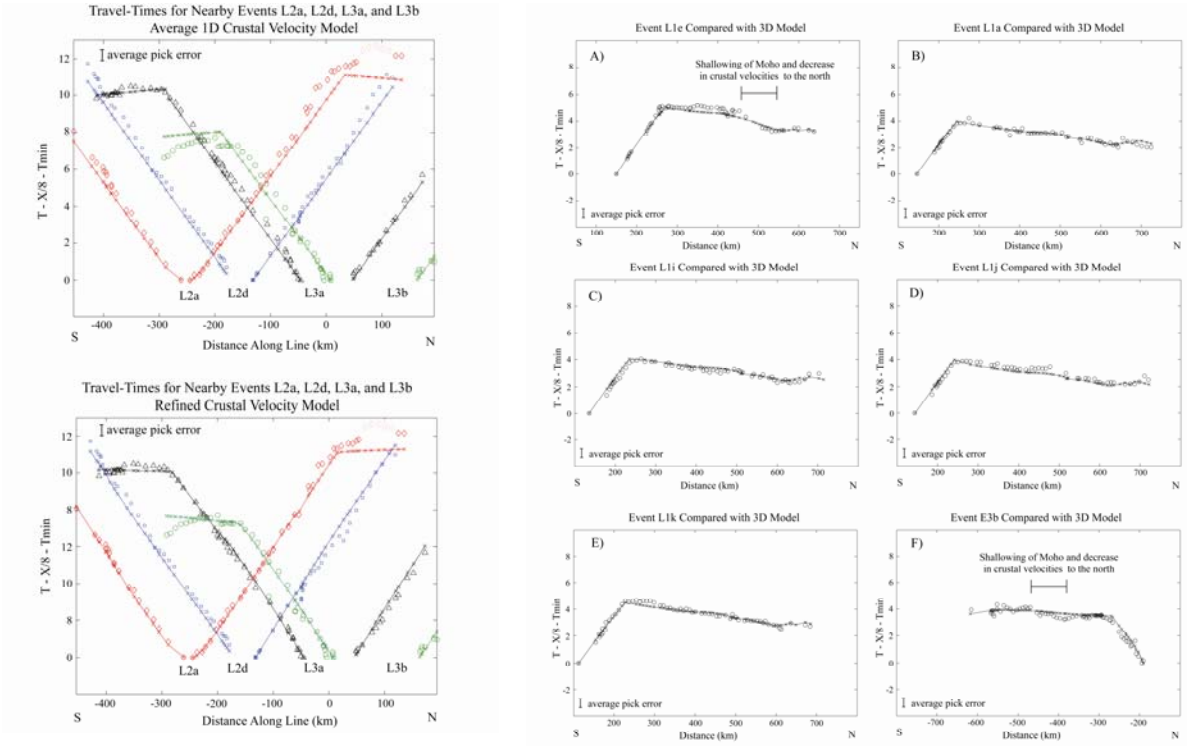

Figure 3. The left two plots show the observed first-arrival travel times and the calculated travel times (lines and crosses) for the relocated nearby events using the average 1D crustal model on top and the refined crustal velocity model on the bottom. The right plots show observed P-wave travel times (circles) and calculated travel times (lines and crosses) for the far-regional events: (A) L1e, (B) L1a, (C) L1i, (D) L1j, (E) L1k, and (F) E3b.

Figure 2 shows ray diagrams calculated using the 3D ray-tracer CRT (Cerveny et al., 1988) for the Event L1e shown by the red circle. The left plot is viewed from the west, and the right plot is viewed from the south. The blue top surface indicates the structure of the Moho used for the 3D model. The left top plot of Figure 3 shows the observed P-wave travel times for the relocated nearby Events L2a, L2d, L3a, and L3b, compared with the calculated travel times using the average 1D crustal velocity model. The left bottom plot of Figure 3 shows the observed travel times

of the first-arrival P waves for the nearby events, compared with the calculated travel times of the refined, laterally varying crustal velocity model. The right plots of Figure 3 show the observed P-wave travel-times (circles) for the far-regional Events (A) L1e, (B) L1a, (C) L1i, (D) L1j, (E) L1k, and (F) E3b. The *Pn* travel-times for these events were used to constrain the Moho structure and *P*-wave velocities in the upper mantle for this part of the Tibetan Plateau. The lines and crosses in each of the far-regional travel-time plots are the calculated travel-times using the inferred 3D regional velocity model.

Figure 4 shows plots of the 3D Moho and upper-mantle velocity structure found in this study from the modeling of near and far regional travel-time data for this region of the Tibetan Plateau, as viewed from (A) the west and (B) the south (Griffin et al, 2010). The upper-mantle velocities are higher and the Moho deeper beneath the southern portion of the plateau south of the Bangong-Nuijang suture (BNS), and upper-mantle velocities are lower and the Moho is shallower north of the BNS. These results are similar to those found by Tseng et al. (2009) using virtual seismic profiles from the *SsPmP* teleseismic phase and by Nowack et al. (2010) using Gaussian beam migration of teleseismic receiver functions. Other structure controls on the structure have been found by Hung et al. (2010) using finite frequency tomography of teleseismic arrival times, and for anisotropic structure of the upper mantle by Chen et al. (2010).

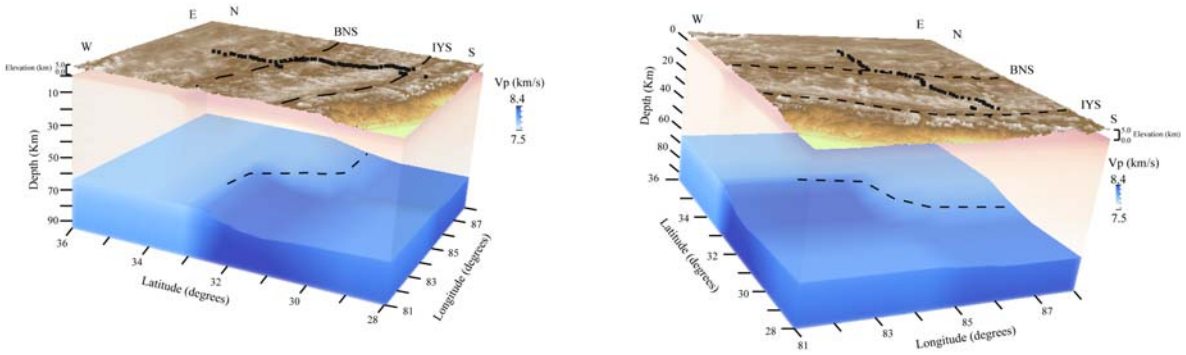

Figure 4. The 3D Moho and upper-mantle velocity structure found in this study for the region of the Hi-CLIMB array, with the left plot showing a view from the west and the right plot showing a view from the south.

The *Pn* phase is typically not a simple head wave but is composed of a complex set of interfering waves when there is a positive velocity gradient with respect to depth below the Moho interface (Cerveny and Ravindra, 1971; Hill, 1971; Menke and Richards, 1980). These interfering waves can also simply result from the spherical nature of the Earth (Hill, 1973; Sereno and Given, 1990, Yang et al., 2007), which gives an effect equivalent to a velocity gradient in a corresponding flattened Earth model. How observed amplitudes of refracted waves change over distance supports the interpretation that these arrivals are composed of diving and interference waves and is in contrast to a pure head wave (Braile and Smith, 1975). To account for the intricate nature of *Pn* propagation, we are applying SEM (Komatitsch and Vilotte, 1998; Komatitsch et al., 2005), as well as asymptotic ray/beam methods. In contrast, alternatives such as the reflectivity method are restricted to 1D media. SEM can be applied in 2D or 3D and implemented in parallel using message passing interface (MPI) on large-cluster computing. Here we are applying a 2D viscoelastic SEM code. As a practical measure, essential features of *Pn* waveforms are being distilled into seismic attributes, including arrival times, envelopes of wave amplitudes, and pulse frequencies for modeling.

To test the effects of upper-mantle velocity gradient, Moho topography, and lateral velocity variation on *Pn* propagation, we designed two velocity models. The left plot of Figure 5 shows the P-wave velocity model for a laterally homogeneous flat model with an upper-mantle velocity gradient of .004 1/s and has a crustal layer above a half space, with the Moho at 70 km depth. The right plot of Figure 5 shows a simplified 2D slice of a model derived from the 3D travel-time modeling, using regional data from the Hi-CLIMB array. Both the crust and the upper mantle have velocity gradients with depth and velocities that change laterally. The Moho changes in depth from 73.4 km on the left side of the model to 64.3 km on the right side of the model.

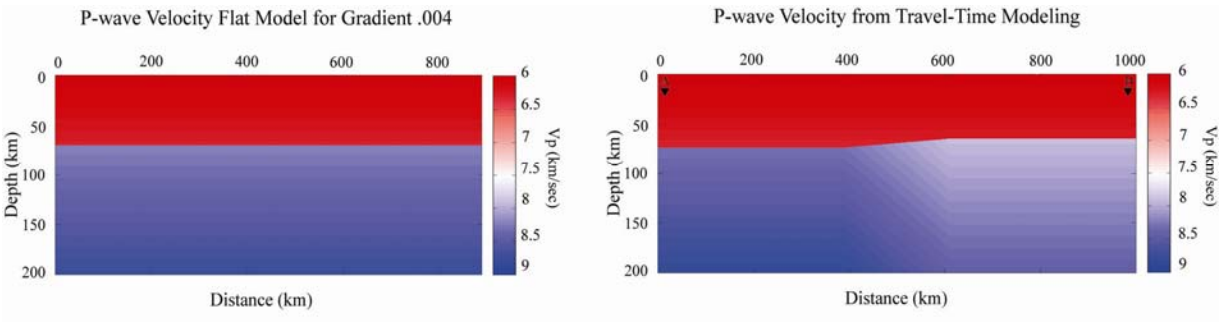

Figure 5. The left plot shows the P-wave velocities for a simple layer over a gradient with an upper-mantle velocity gradient of .004 1/s. The right plot shows a simplified P-wave velocity model from travel-time modeling of regional events from Hi-CLIMB, showing a step in the Moho.

Figure 6 shows the first arrival amplitudes for several laterally homogeneous models with different upper-mantle velocity gradients of 0, 0.002, 0.004, and 0.006 1/s. The case where the upper-mantle gradient is .004 1/s is the model shown in Figure 5 (left plot). As seen in Figure 6, when there is no upper mantle gradient, the *Pn* pulse amplitudes decrease with distance from 300 to 800 km. For an upper-mantle velocity gradient greater than .004, the *Pn* pulse amplitudes increases for this distance range.

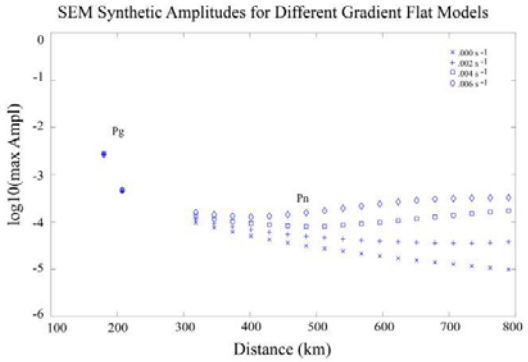

Figure 6. SEM synthetic P-wave amplitudes for several velocity models with different upper-mantle velocity gradients of 0.0, 0.002, 0.004, and 0.006 1/s.

Figure 7 shows the amplitudes computed for the velocity model shown in the right plot of Figure 5, with a step in the Moho that approximately satisfies the general shape of the Hi-CLIMB travel-time data. The blue curve is for source B near 1000 km and recorded to the south in Figure 5 (right plot); the red curve is for source A near 0 km and recorded to the north in Figure 5 (right plot). The synthetic amplitudes suggest that the amplitudes should relatively increase with distance for the *Pn* branch for source B, resulting from the step in the Moho for the particular upper-mantle velocity gradient. However, for source A, the *Pn* amplitudes should relatively decrease with amplitude, resulting from the step in the Moho. Thus, using events at different locations to the north and south of the Hi-CLIMB array, one should be able to identify the large-scale structural features.

In order to analyze the amplitude and pulse frequency data from Hi-CLIMB, we must first define several 2D cross sections from the derived 3D velocity model from travel-time modeling in order to compare with the 2D SEM results. In addition, an Earth-flattening transformation must be applied to use the 2D SEM modeling. Also, the 2D SEM amplitudes must be approximately corrected for out-of-plane spreading to compare with the observed amplitude data. The locations of the cross sections are shown in map view in Figure 1. The West Line along 84 degrees, Central Line along 85 degrees, and East Line along 86 degrees are used to model seismic attributes for event gathers L1e, group (L1a, L1i, L1j, L1k), and E3b, respectively. The earth-flattened models along these three lines are shown in Figure 8.

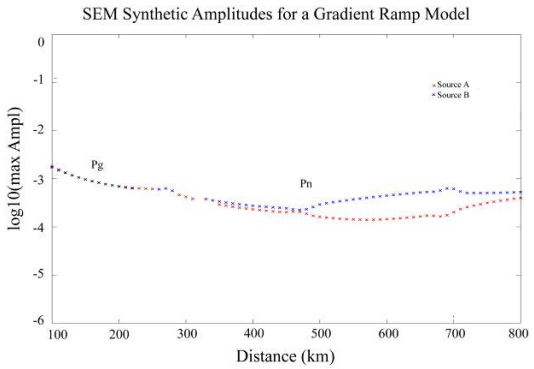

Figure 7. SEM synthetic amplitudes for a step in the Moho, as shown for the right plot in Figure 5. The blue curve is for source B near 1000 km in Figure 5 (right plot) and recorded to the south, and the red curve is for source A near 0 km and recorded to the north in Figure 5 (right plot).

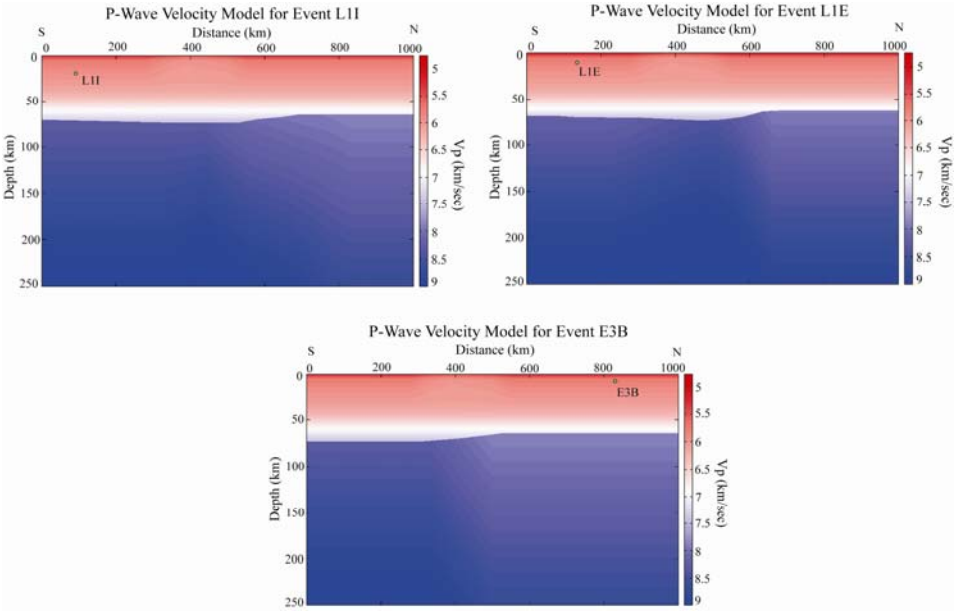

Figure 8. The top left plot shows the Earth-flattened Central Line through the 3D velocity model for Event L1i, the top right plot shows the Earth-flattened West Line though the 3D velocity model for Event L1e, and the lower plot shows the Earth-flattened East Line through the 3D velocity model for Event E3b.

We initially need to match the observed travel times on each event gather using the approximate 2D slices that have been Earth flattened. The upper left plot of Figures 9 and 10 show the travel-time comparisons for Events L1i and L1e, respectively. As can be seen in the travel-time comparisons, the 2D SEM calculations with the models given in Figure 8 do a reasonably good job at fitting the travel times.

For the upper right plots in the Figures 9–10, the observed Hilbert envelope amplitudes for the P-wave pulses are then compared with those calculated from the 2D SEM code. In order to make the comparison with the observed data, the 2D amplitudes are approximately corrected to account for out-of-plane spreading. However, for future research these results will need to be compared with 3D SEM calculations. For Events L1i and L1e, the *Pn* waves across the Moho step from a deeper Moho to a shallower Moho. From the synthetic results shown in Figure 7, this will result in a lowering in the amplitudes at larger offsets, resulting from the large-scale structural effects for events to the south. From the observed amplitudes for Events L1i and L1e shown in Figures 9 and 10, there are relatively

lower amplitudes at offsets between 500 to 600 km. Note that the observed amplitudes were only selected if there was no interference with later arrivals, and also reliable pulse frequencies could be estimated.

The SEM modeling includes the finer-scale upper-mantle velocity gradients that are initially taken from the 3D velocity model and are similar to those found by Phillips et al. (2007). The velocity gradients are also similar to those found by Myers et al. (2010) in the southern Lhasa terrane but are larger than those given by Myers et al. (2010) for the northern Qiangtang terrane. However, the upper-mantle speeds from the travel-time modeling of Hi-CLIMB *Pn* data are more similar to the results found by Phillips et al. (2007), as well as to other recent travel-time modeling studies on the Tibetan Plateau, including Liang and Song (2006), Sun and Toksoz (2006), and Hearn et al. (2004).

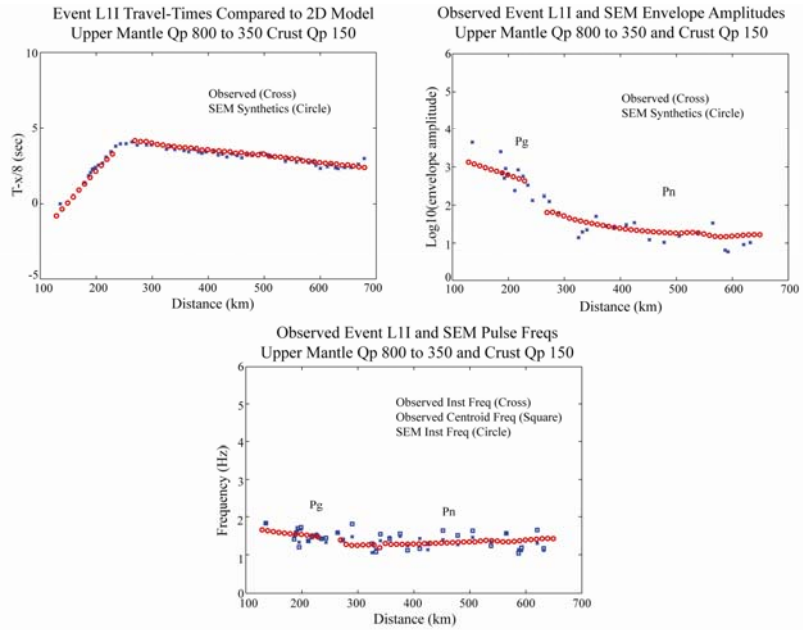

Figure 9. Seismic attribute comparisons for Event L1i between observed and calculated SEM attributes. The travel times are shown in the upper left plot, the pulse amplitudes are shown in the upper right plot, and the pulse frequencies are shown in the lower plot.

For the Lhasa terrane in the southern Tibet, the structural velocity model seems to account for a good portion of the amplitude signature for Events L1i and L1e, with larger Q values to the south of the BNS. However, the upper-mantle Q values for the Qiangtang terrane are around 350 for the L1I an L1E profiles at frequencies near 1.5 Hz. For Event E3b, we are still re-evaluating the focal mechanism, but initial modeling has somewhat lower upper mantle Q values in the Qiangtang terrane at frequencies near 1.5 Hz. These variations can be related to different ray paths for Event E3b to the north and for Events L1i and L1e to the south (Figure 1). Nonetheless, these upper-mantle Q values for the Qiangtang terrane are consistent with the range of Q values found by Xie (2007).

The pulse-broadening estimates are shown in the lower plots of Figures 9–10, where the observed values are given for both the instantaneous and spectral centroid frequencies. The calculated pulse frequencies are shown using the instantaneous frequencies. In Figures 9 and 10, the pulse frequencies are shown for Events L1i and L1e, and a reasonably good agreement is found between the observed and calculated values. For Event E3b, there are still some slight discrepancies with the calculated pulse frequency values for the *Pn* branch, which are somewhat higher than the observed values. This discrepancy might suggest a somewhat-lower upper-mantle velocity gradient in the northern Qiangtang terrane, possibly more similar to that found by Myers et al. (2010). However, this might also decrease the calculated amplitudes compared to the observed values. In any case, further tests on this are being investigated, and the focal mechanism for Event E3b is also being re-evaluated.

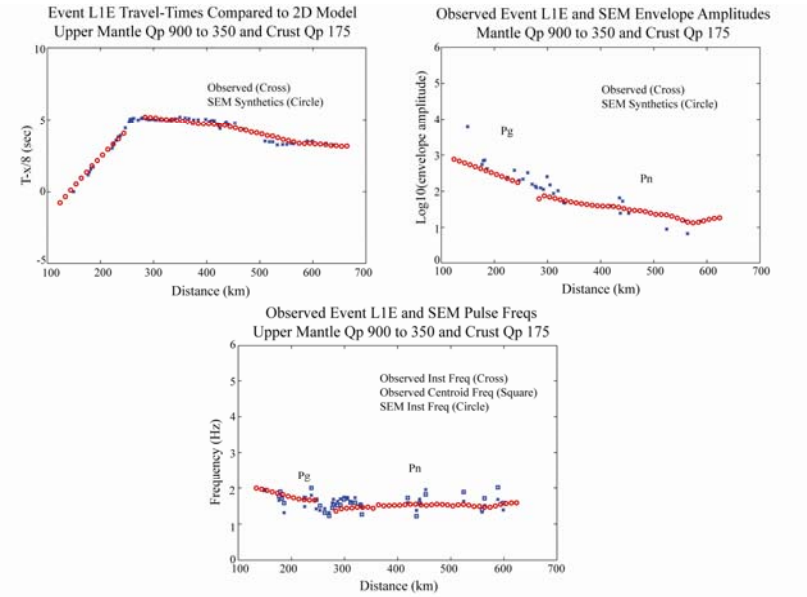

Figure 10. Seismic attribute comparisons for Event L1e between observed and calculated SEM attributes. The travel times are shown in the upper left plot, the pulse amplitudes are shown in the upper right plot, and the pulse frequencies are shown in the lower plot.

CONCLUSIONS AND RECOMMENDATIONS

We have assembled a number of record sections from regional events recorded by the Hi-CLIMB array. For several events nearby the Hi-CLIMB array, we have relocated the events using Hi-CLIMB data. From these record sections, seismic attributes of the *Pn* phase have been extracted from the data, including arrival times, envelope amplitudes, and instantaneous and spectral pulse frequencies. Several nearby events to the Hi-CLIMB array have been used to constrain crustal velocities from the crustal branches. For the *Pn* phases, the travel times have been modeled using 3D ray tracing in order to constrain the large-scale structural features, including Moho depths, upper-mantle velocities, and velocity gradients. Numerical modeling has been performed using SEM for selected regional event gathers in order to estimate the effects of large-scale velocity structure and attenuation on the extracted seismic attributes.

REFERENCES

Baur, J. R. (2007). Seismotectonics of the Himalayas and the Tibetan Plateau: Moment tensor analysis of regional seismograms, M.S. thesis, Oregon State University.

Braile, L. W. and R. B. Smith (1975). Guide to the interpretation of crustal refraction profiles, *Geophys. J. R. Astr. Soc.* 40: 145–176.

Cerveny, V., L. Klimes, and I. Psencik (1988). Complete seismic-ray tracing in three-dimensional structures, in *Seismological Alogorithms.* London: Academic Press.

Cerveny, V. and R. Ravindra (1971). *Theory of Seismic Head Waves*. University of Toronto Press.

Chen, W. P. M. Martin, T. L. Tseng, R. L. Nowack, S. Hung, and B. Huang (2010). Shear-wave birefringence and current configuration of converging lithosphere under Tibet, *Earth Planet. Sci. Lett.*, 295, 297-304.

Chen, W.-P., and P. Molnar (1983). Focal depths of intracontinental and intraplate earthquakes and their implications for the thermal and mechanical properties of the lithosphere, *J. Geophys. Res.* 88: 4183–4214.

Dziewonski, A. M., T.-A. Chou and J. H. Woodhouse (1981). Determination of earthquake source parameters from waveform data for studies of global and regional seismicity, *J. Geophys. Res.* 86: 2825–2852.

Engdahl, E. R., R. D. van der Hilst, and R.P. Buland (1998). Global teleseismic earthquake relocation with improved travel times and procedures for depth determination, *Bull. Seism. Soc. Am.* 88: 722–743.

Griffin, J. D., R. L. Nowack, T. L. Tseng, and W. P. Chen (2010). Modeling of three-dimensional regional velocity structure using wide-angle seismic data from the Hi-CLIMB experiment in Tibet, *Seism. Res. Lett.* 81: 373.

Hearn, T. M., S. Wang, J. F. Ni, Z. Xu, Y. Yu, and X. Zhang (2004). Uppermost mantle velocities beneath China and surrounding regions, *J. Geophys. Res.* 109: B11301.

Hill, D. (1971) Velocity gradients and anelasticity from crustal body-wave amplitudes, *J. Geophys. Res.* 76: 3309–3325.

Hill, D. (1973). Critically refracted waves in a spherically symmetric radially heterogeneous Earth model, *Geophys. J. R. Astr. Soc.* 34: 149–177.

Hung, S. H., W. P. Chen, L. Y. Chiao, and T. L. Tseng (2010). First multi-scale, finite frequency tomography illuminates 3-D anatomy of the Tibetan Plateau, *Geophys. Res. Lett.* 37: doi:10.1029/2009GL041875.

Klein, F. (2002). HYPOINVERSE-2000 (4/2002 vers.) [Computer Software]. Menlo Park, CA: U.S. Geological Survey.

Komatitsch, D. and J. P. Vilotte (1998). The spectral element method: An efficient tool to simulate the seismic response of 2D and 3D geological structures, *Bull. Seismol. Soc. Am.* 88: 368–392.

Komatitsch, D., S. Tsuboi, and J. Tromp (2005). The spectral-element method in seismology, in *Seismic Earth: Array Analysis of Broadband Seismograms*, Geophysical Monograph Series, Vol. 157, A. Levander and G. Nolet, Eds. Washington, DC: American Geophysical Union.

Liang, C. and X. Song (2006). A low velocity belt beneath northern and eastern Tibetan Plateau from *Pn* tomography, *Geophys. Res. Lett.* 33: L22306.

Langin, W. R., L. D. Brown, and E. A. Sandvol (2003). Seismicity of central Tibet from Project INDEPTH III seismic recordings, *Bull. Seism. Soc. Am.* 93: 2146–2159.

Menke, W. H. and P. G. Richards (1980). Crust-mantle whispering gallery phases—A deterministic model of teleseismic Pn wave-propagation, *J. Geophys. Res.* 85: 5416–5422.

Molnar, P. and W.-P. Chen (1983). Depths and fault plane solutions of earthquakes under the Tibetan plateau, *J. Geophys. Res.* 88: 1180–1196.

Myers, S. M. L. Begnaud, S. Ballard, M. E. Pasyanos, W. S. Phillips, A. L. Ramirez, M. S. Antolik, K. D. Hutchenson, J. J. Dwyer, C. A. Rowe, and G. S. Wagner (2010). A crust and upper-mantle model of Eurasia and North Africa for *Pn* travel-time calculation, *Bull. Seism. Soc. Am.* 100: 640–656.

Nabelek, J., W. P. Chen, M. R. Pandey, J. Mei, J. Chen, B. S. Huang, and the Project Hi-CLIMB Team (2005). Hi-CLIMB: A high-resolution seismic profile across the Himalayas and Southern Tibet, IRIS Annual Report, Washington DC.

Nowack, R. L., W .P. Chen, and T. L. Tseng (2010). Application of Gaussian beam migration to multi-scale imaging of the lithosphere beneath the Hi-CLIMB array in Tibet, *Bull. Seism. Soc. Am.* 100: 1743–1754.

Phillips, W. S., M. L. Begnaud, C. A. Rowe, L. K. Steck, S. C. Myers, M. E. Pasyanos, and S. Ballard (2007). Accounting for lateral variations of the upper mantle gradient in *Pn* tomography studies, *Geophys. Res. Lett.* 34: doi:10.1029/2007GL029338.

Sereno, T. J. and J. W. Given (1990), *Pn* attenuation for a spherically symmetric Earth model, *Geophys. Res. Lett.* 17: 1141–1144.

Sun, Y. and M. N. Toksoz (2006). Crustal structure of China and surrounding regions from *P*-wave travel-time tomography, *J. Geophys. Res.* 111: B03310.

Tseng, T. L., W. P. Chen, and R .L. Nowack (2009). Northward thinning of the Tibetan crust revealed by virtual seismic profiles, *Geophys. Res. Lett.* 36: L244304, doi:10.1029/2009GL040457.

Xie, J. (2007). *Pn* attenuation beneath the Tibetan Plateau, *Bull. Seism. Soc. Am.* 97: 2040–2052.

Yang, X., T. Lay, X. B. Xie, and M. S. Thorne (2007). Geometric spreading of *Pn* and *Sn* in a spherical earth model, *Bull. Seism. Soc. Am.* 97: 2053–2065.